Journal of Materials Chemistry A

Accepted Manuscript

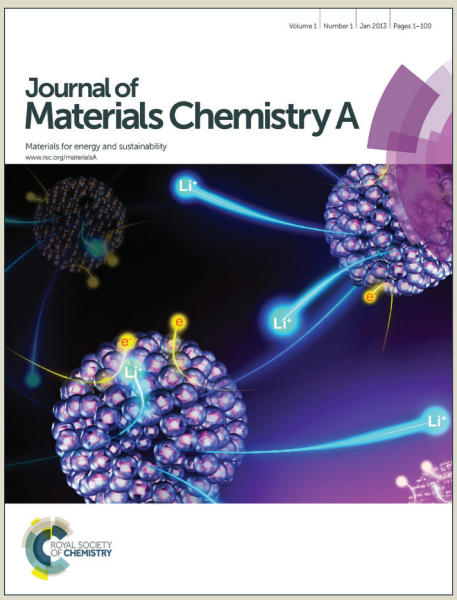

ROYAL SOCIETY OF CHEMISTRY

www.rsc.org/materialsA

Journal Name

RSCPublishing

ARTICLE

Facile fabrication of hierarchical porous rose-like $NiCo_2O_4$ nanoflake/$MnCo_2O_4$ nanoparticle composite with enhanced electrochemical performance for energy storage

Cite this: DOI: 10.1039/x0xx00000x

Received 00th January 2012,
Accepted 00th January 2012

DOI: 10.1039/x0xx00000x

www.rsc.org/

Yanjun Zhai,[†] Hongzhi Mao,[†] Peng Liu,[†] Xiaochuan Ren,[‡] Liqiang Xu,[†,*] and Yitai Qian[†,§]

The rational design of three-dimensional (3 D) hierarchical porous architectures possessing the advantages of improved electrical conductivity and reduced volume change during the charge/discharge processes has been proved to be an effective way for enhancing the electrochemical performance of binary metal oxides and related hybrids. Herein, uniform 3D hierarchical porous rose-like $NiCo_2O_4$/$MnCo_2O_4$ is controllably fabricated through a facile hydrothermal process followed by a subsequent heat treatment, which exhibits high cycling stability (1009 mA h g^{-1} at 1000 mA g^{-1} after 600 cycles), high specific capacity and excellent rate capability as anodes for lithium ion batteries; In addition, the $NiCo_2O_4$/$MnCo_2O_4$ displays an initial specific capacitance of 911.3 F g^{-1} as supercapacitor electrode at 5 A g^{-1}. Its excellent electrochemical performances may originate from the unique hierarchical and porous structure, which can buffer the volume expansion and increase the contact area between the electrode and electrolyte. The as-obtained 3D hierarchical porous rose-like $NiCo_2O_4$/$MnCo_2O_4$ composite exhibits outstanding electrochemical performances, which is a promising candidate for the next-generation energy storage electrode.

1 Introduction

Advanced electrode materials play key roles on the improvement of renewable power sources such as lithium ion rechargeable batteries (LIBs) and supercapacitors (SCs), and extensive efforts have been focused on their rational designation in order to enable them with higher energy density, higher power density and long cycling stability during the past decades.[1,2] Transition-metal oxides such as iron-based oxides[3,4], cobalt-based oxides[5-7] and manganese-based oxides[8,9] have been widely utilized as promising advanced electrode materials for energy storage applications. Among them, cobalt-based binary oxide nanomaterials with porous characteristics have recently attracted increasing attention as electrode materials for LIBs and SCs. For example, $NiCo_2O_4$@Au nanotubes with mesoporous structure have high-performances as LIBs (732.5 mA h g^{-1} remained after 200 th cycles at 100 mA g^{-1}) and SCs (~ 861 F g^{-1} maintained after 10,000 cycles at 5 A g^{-1});[5] mesoporous flake-like $MnCo_2O_4$ is investigated as an anode material for LIBs and as an electrode material for supercapacitors, exhibiting a reversible capacity of 952 mA h g^{-1} at 100 mA g^{-1} after 100 cycles and 93.3% of the initial specific capacitance retained at 50 mV s^{-1} after 2000 cycles, respectively;[6] $Zn_xCo_{3-x}O_4$ hollow polyhedral demonstrate a remarkable high-rate performance, which is significantly superior to that of most $ZnCo_2O_4$ nanostructures reported previously.[7] The cycle performances of these cobalt-based oxides anodes have been greatly improved. However, the capacity fade and poor rate capability are still key challenges and issues faced by us today.

Metal oxides with porous and multicomponent hierarchical nanostructure features could buffer volume variation, address the low bulk density and take full advantages of different components.[10-13] For instance, Fe_2O_3@$NiCo_2O_4$ porous nanocages for LIBs exhibited a high initial discharge capacity of 1311.4 mA h g^{-1} at 100 mA g^{-1};[11] mesoporous NiO/$NiCo_2O_4$/Co_3O_4 composite for SCs displayed high specific capacitance (1717 F g^{-1}) and electrochemical stability (94.9% retention after 1000 cycles);[12] $NiCo_2O_4$/hierarchical porous carbon composite as electrode for LIBs shows a reversible capacity of 660 mA h g^{-1} after 500 cycles at 1000 mA g^{-1}.[13] Therefore, metal oxides with porous and multicomponent

hierarchical nanostructures are expected to show enhanced electrochemical properties. Previously, individual spinel structured $NiCo_2O_4$ (electrical conductivity: 0.1–0.3 S cm^{-1})[14] or $MnCo_2O_4$[6] has been proved to be promising electrode material for LIBs and SCs. However, to the best of our knowledge, there is no report on the rational design of 3D hierarchical porous double binary metal oxide ($NiCo_2O_4$/$MnCo_2O_4$) architectures as advanced and high performance electrode materials for LIBs and SCs until now.

In this report, hierarchical porous rose-like $NiCo_2O_4$ nanoflake/$MnCo_2O_4$ nanoparticle composite has been fabricated by a facile hydrothermal synthesis and a post-annealing treatment. When evaluated as anode material for LIBs, the composite exhibits high specific capacity, excellent rate capability and cycling stability (1009 mA h g^{-1} at 1000 mA g^{-1} after 600 cycles); When applied as supercapacitor electrode, its specific capacitance reaches 911.3 F g^{-1} at 5 A g^{-1}. All of these results indicate its good potential applications for LIBs and SCs.

2 Experimental

2.1 Preparation of 3D hierarchical porous rose-like $NiCo_2O_4$ and $NiCo_2O_4$/$MnCo_2O_4$.

All of the chemical reagents were of analytical grade without purification. The 3D hierarchical porous rose-like $NiCo_2O_4$ was synthesized as follows: in a typical procedure, 1 mmol of $Ni(NO_3)_2 \cdot 6H_2O$ and 2 mmol of $Co(NO_3)_2 \cdot 6H_2O$ were dissolved into a mixed solvent of de-ionized (DI) water (20 mL) and ethanol (10 mL) at room temperature (RT) to form a transparent pink solution, followed by addition of 10 ml of trolamine (TEA). The whole mixture was stirred for another 20 min to obtain a homogeneous solution. Then the resulting solution was transferred into a Teflon-lined stainless steel autoclave (60 ml capacity), which was sealed and heated to 180 °C for 12 h. After the autoclave was cooled to room temperature naturally, the resulting product was rinsed with DI water and absolute ethanol for several times. Then the product was collected and dried at 60 °C for 12 h in air. This was named the Ni-Co-based precursor. Furthermore, the as-obtained Ni-Co-based precursor was further put into a 60 mL Teflon-lined stainless steel autoclave containing 1.6 mM $KMnO_4$ solution, which was subsequently heated and maintained at 160 °C for 30 min. The sample was collected, washed with DI water and ethanol, and then dried at 60 °C to obtain hierarchical Ni-Co-Mn-based precursor. Finally, the as-prepared hybrid product was annealed at 350 °C with a temperate ramp rate of 0.5 °C min^{-1} for 2 h to obtain hierarchical $NiCo_2O_4$/$MnCo_2O_4$. The as-obtained Ni-Co-based precursor was annealed at the same condition to obtain hierarchical porous rose-like $NiCo_2O_4$.

2.2 Characterization

The X-ray powder diffraction (XRD) patterns were obtained from a Bruker D8 advanced X-ray diffractometer equipped with graphite-monochromatized CuKα radiation. The morphology and structure of the samples were observed through a field emission scanning electron microscope (FESEM, ZEISS SUPRA-55) and the transmission electron microscopy (TEM, JEM-2011). Energy dispersive spectrometer (EDS, 200 kV) instruments, X-ray photoelectron spectroscopy (XPS, ESCALAB 250) and Raman spectra (LabRAM HR800) were also conducted to determine the compositions of the as-obtained samples. A certain amounts of the $NiCo_2O_4$/$MnCo_2O_4$ and $NiCo_2O_4$ were placed in a small measuring cylinder and tapped for at least 90 min by hand to measure the tap density. The mass and the measured volume of the tapped powder were used to calculate their tap density.

2.3 Electrochemical measurements

The electrochemical tests versus Li were measured on a Land battery test system (CT2001A, Xinnuo, Wuhan China) at room temperature. The electrode was made by pasting mixed slurry that consisted of active materials, Sodium Carboxy Methyl Cellulose (CMC), and carbon black (50 wt% : 30 wt% :20 wt% and 70 wt% : 20 wt% : 10 wt%) onto a copper foil. The electrodes were dried in vacuum oven at 60 ℃ for 12 h. The separator was a Celgard 2300 microporous polypropylene membrane and the current collector was Nickel foam. The electrolyte used in the cells was 1 M LiPF6 in an ethylene carbonate/dimethyl carbonate/diethyl carbonate (EC/DMC/DEC, 1:1:1 w/w). Lithium foil was used as counter electrode. The coin cells of type CR2032 were assembled in an argon-filled glove box. Galvanostatic discharge/charge was cycled in the voltage range of 0.01-3.0 V (vs. Li^+/Li). The cyclic voltammetry (CV) profiles were carried out in the potential window of 0.01 to 3.0 V by an electrochemical workstation (LK2005, Lanlike, Tianjin China). Electrochemical impedance spectroscopy (EIS) was carried out on an electrochemical workstation (Materials Mates 510, Italia) in the frequency range from 0.1 MHz to 0.01 Hz, applying a 5 mV bias voltage. Direct current resistance (R_{dc}) was measured at a pulse of 18 s at every 5% increase of depth of discharge and state of charge. Then, the DC resistance could be obtained by $R_{dc}=\Delta U/I$, where ΔU is the voltage variation before and after the interruption, and I is the current.

For the electrochemical measurements of supercapacitors, the working electrodes were constructed by mixing the active material, acetylene black and a polyvinylidene fluoride (PVDF) binder. $NiCo_2O_4$/$MnCo_2O_4$ (80%), acetylene black (10%) and the PVDF binder (10%) were dispersed in an N-methyl-2-pyrrolidinone (NMP) solvent and ground thoroughly to form homogeneous slurries, and then, the slurries were coated on the nickel foam substrates (surface, 1.2 cm × 1.2 cm). After being dried at 80°C for 4 h to remove the solvent, the as-formed electrodes loaded with the active material were then pressed at 10 MPa. Before and after the sample was dried thoroughly, the nickel foam was weighed. The mass loading of active materials in a nickel foam electrode was about 3.0 mg. The obtained $NiCo_2O_4$/$MnCo_2O_4$ modified electrode was then used as a working electrode. The reference electrode and counter electrode were saturated calomel reference electrode (SCE) and platinum foil, respectively. All electrochemical measurements

were performed using an electrochemical working station (CHI760e, Shanghai, China) in 2 M KOH aqueous solution at 25 °C.

3 Results and discussion

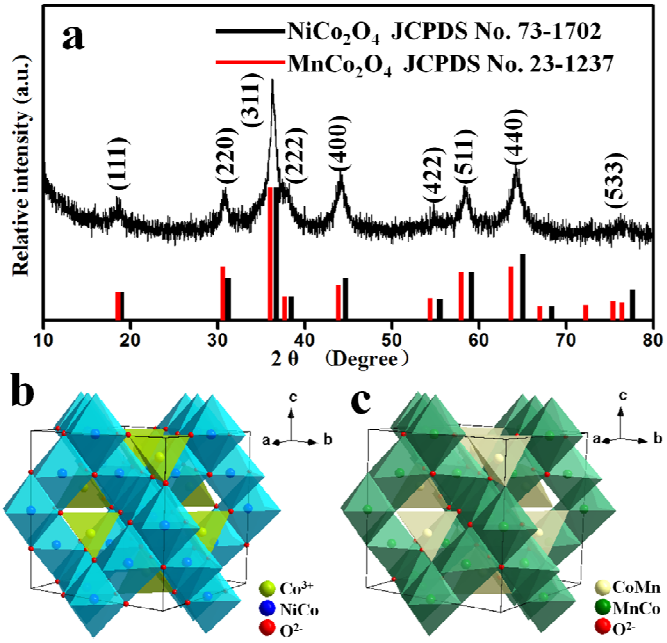

Fig. 1 (a) XRD patterns of as-prepared $NiCo_2O_4/MnCo_2O_4$ and (b,c) structure illustration of spinel $NiCo_2O_4$ and $MnCo_2O_4$.

Hierarchical 3D porous rose-like $NiCo_2O_4/MnCo_2O_4$ and $NiCo_2O_4$ can be obtained by calcining Ni-Co-Mn-based precursors and Ni-Co-based precursors at 350 °C for 2 h (the related SEM, TEM and EDX mapping images are shown in Fig. S1), respectively. Thermogravimetric analysis (TGA) is conducted to investigate the thermal decomposition behavior of the Ni-Co-Mn-based precursor. Fig. S2 shows that the Ni-Co-Mn-based precursors have a sharp weight loss between 200 and 250 °C. Therefore, the Ni-Co-Mn-based precursors were calcined at 350 °C for 2 h to obtain the final products. A representative X-ray diffraction (XRD) patterns of the as-prepared final products is shown in Fig. 1a. All of the diffraction peaks can be indexed and assigned to $NiCo_2O_4$ [JCPDS card no. 73-1702, a=8.114 Å, space group Fd 3 m (227)] or/and $MnCo_2O_4$ [JCPDS card no. 23-1237, a=8.269 Å, space group Fd3m (227)].[6,15] There are no impurity peaks such as Mn_xO_y observed in the product. The diffraction peaks of the product (obtained after the Ni-Co-based precursors were calcined at 350 °C for 2 h) (Fig. S3) can be indexed to $NiCo_2O_4$ (JCPDS card no. 73-1702), and no impurities are found in this XRD pattern. The parameters of the composite and individual two binary metal oxide XRD patterns are displayed in Tab. S1, revealing the slight displacement shifting phenomenon. Crystallographic structure of $NiCo_2O_4$ (Fig. 1b) shows that the nickel ions occupying the octahedral sites, while in the $MnCo_2O_4$ (Fig. 1c), the manganese ions are distributed in tetrahedral and octahedral sites.[15,16] The Raman spectra (Fig. S4 and Tab. S2) of $NiCo_2O_4/MnCo_2O_4$ displays that no detectable peaks that related to manganese oxides in the products.[17-21] It is found that the peak centered at 690 cm^{-1} corresponding to individual $NiCo_2O_4$ could not be clearly observed in the $NiCo_2O_4/MnCo_2O_4$ composite, instead of it, an obvious peak with high intensity is observed at 622 cm^{-1}. It is considered that the experimental parameters (such as the temperature or treatment process for the product) and structure of the composite may play important roles for arousing the frequency shifts and band broadening of the Raman behavior,[22] however, the exact reason still needs further research. This result is consistent with that of the XRD patterns (Fig. 1a). Elemental composition analysis of the mixed oxides obtained from energy dispersive spectrometer (EDS) further certificates the existence of nickel, cobalt, manganese and oxygen element (Fig. S5).

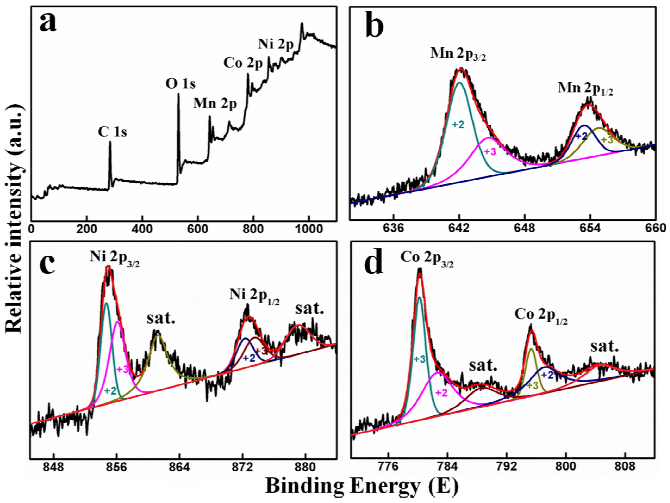

Fig. 2 XPS spectra of (a) the survey spectrum, (b) Mn 2p, (c) Ni 2p and (d) Co 2p spectra of the hierarchical porous rose-like $NiCo_2O_4/MnCo_2O_4$.

In order to investigate the surface composition and the metallic state of the product, X-ray photoelectron spectroscopy (XPS) spectra of $NiCo_2O_4/MnCo_2O_4$ sample was carried out (Fig. 2). The full XPS spectrum (Fig. 2a) evidences the existence of Ni (Ni 2p1/2, Ni 2p3/2), Co (Co 2p1/2, Co 2p3/2), Mn (Mn 2p1/2, Mn 2p3/2), O (O 1s), and C elements. Among them, the Ni 2p, Co 2p and Mn 2p spectras are fitted with the XPSPEAK41 software and shirley-type background. As shown in Fig. 2b, the Mn 2p3/2 peak is centered at 642.1 eV and the Mn 2p1/2 peak is centered at 653.7 eV, which could be divided into four subpeaks: two of them that centred at 641.8 and 653.2 eV are attributed to the binding energy of Mn^{2+}, while other two at 643.4 and 654.2 eV are assigned to the signal of Mn^{3+}.[23] The high-resolution spectrum for the Ni 2p region (Fig. 2c) is fitted with two spin-orbit doublets, characteristic of Ni^{2+} and Ni^{3+}, and two Shakeup satellites (denoted as "Sat."). The Co 2p emission spectrum (Fig. 2d) is also fitted with two spin-orbit doublets, characteristic of Co^{2+} and Co^{3+}, and one shakeup satellite.[13,24] These results show that the chemical composition of final product contains Co^{2+}, Co^{3+}, Ni^{2+}, Ni^{3+}, Mn^{2+} and Mn^{3+}, which are in good agreement with the results in the literature for $NiCo_2O_4/MnCo_2O_4$.

Journal Name

RSCPublishing

ARTICLE

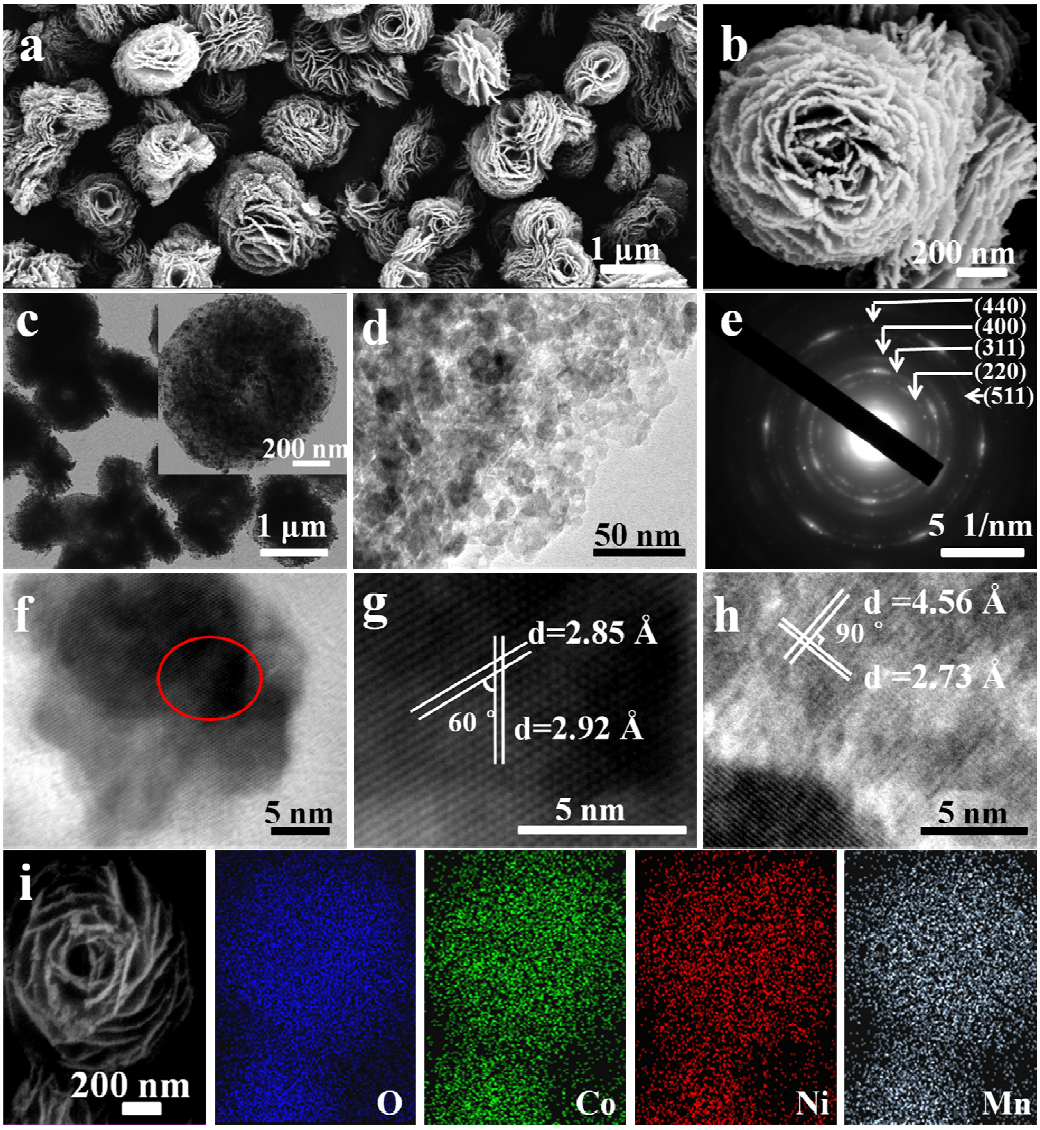

Fig. 3 (a,b) SEM images, (c,d) TEM images, (e) SAED image of $NiCo_2O_4/MnCo_2O_4$, (f) HRTEM image of the $MnCo_2O_4$, (g) HRTEM image of the region marked by the red frame in (f), (h) HRTEM image of the $NiCo_2O_4$ and (i) EDX mapping images of the hierarchical rose-like $NiCo_2O_4/MnCo_2O_4$.

Fig. 3(a-d) shows that the $NiCo_2O_4/MnCo_2O_4$ composite has a hierarchical structure with a size of ~1 μm. The obtained products are constructed by many nanoflakes, generally pointing outward radially and resulting in the rose-like nanostructure. It is clear that the hierarchical rose-like nanostructures are shape remained after calcination. Meanwhile a large number of small pores can be clearly observed on the surface of the nanoplates (Fig. 3d). In addition, the neighboring nanoflakes are loosely interconnected and the space between them obviously exists, which allow easy penetration of the electrolyte.[24,25] The lattice fringes in selected area electron diffraction (SAED) patterns (Fig. 3e and Tab. S3) of $NiCo_2O_4/MnCo_2O_4$ are readily indexed to the interplanar spacing of cubic $NiCo_2O_4$ and $MnCo_2O_4$ structure.[26,27] The HRTEM images (Fig. 3f and Fig. 3g) of a randomly selected $MnCo_2O_4$ nanoparticle reveal that the lattice fringes are 2.85 and 2.92 Å, which match well to the (220) and (022) plans of the cubic $MnCo_2O_4$, respectively. The angle between the two planes is 60 ℃, which is very consistent with the calculated value. In the nanosheet regions (Fig. 3h), two groups of crystal planes (an angle of 90 °) show lattice spacings of 2.73 and 4.56 Å, corresponding to the (220) and (111) planes

of $NiCo_2O_4$ crystals, respectively. For comparison, the morphology of the pure $NiCo_2O_4$ was investigated by TEM and SEM (Fig. S6). Energy dispersive X-ray (EDX) mapping spectroscope (Fig. 3i) shows that the elements of Co, Ni, Mn and O are uniformly distributed in the whole nanoflower, confirming the highly uniform distribution of $NiCo_2O_4$ and $MnCo_2O_4$ in the composite. $MnCo_2O_4$ nanoparticle attached on $NiCo_2O_4$ nanoplate composite could enhance the tap density of electrode materials, which is directly related to the volumetric energy density of a battery. The tap density of $NiCo_2O_4/MnCo_2O_4$ and $NiCo_2O_4$ are about 0.51 and 0.32 g cm^{-3}, respectively.

In order to investigate the formation process of the rose-like Ni-Co-based precursors, time-dependent experiments were performed and the products were analyzed by TEM (Fig. S7). It is found that no noticable precipitate was obtained within 30 min. Then only a small amount of wrinkled nanoflakes with size of ~ 500 nm was formed after 40 minutes (Fig. S7a and S7b). After increasing the solvothermal reaction time to 50 minutes, rose-like nanostructures (with size of 500-700 nm) only consist of few "petals" (Fig. S7c and S7d). After 5 h reaction, small amount of underdeveloped rose-like architectures co-existed with rose-like architectures (see Fig. S7e and S7f) formed, demonstrating their oriented attachment and growth process. When the growth time was extended to 12 h, well-defined rose-like nanostructures (Fig. S7i and S7j) with high yield were produced. However, part of them collapsed and individual nanosheets appeared if the reaction time was prolonged to 15 h (Fig. S7k and S7l). Besides the reaction time, it is also found that the amounts of TEA resulted in the products with different shape. When 0, 3, 6 and 10 ml TEA was added, the shape evolution from irregular nanoplates to regular rose-like nanostructures was occurred (Fig. S8). The above results reveal that nanoscaled layers tend to grow with progressively increasing angles to the radial axis and finally self-assemble into hierarchical fashion along with the increasing reaction time in order to reduce the total surface energy, and the TEA plays crucial guiding roles and steric effects during the growth of rose-like Ni-Co-based precursors.[26,28,29] The possible growth processes of the rose-like Ni-Co-based precursors is shown in Fig. S8e. The specific surface area and average pore size of materials for LIBs and SCs play significant roles in enhancing electrochemical performance. The porous feature of $NiCo_2O_4/MnCo_2O_4$ is also verified by nitrogen adsorption–desorption isotherm. As shown in Fig. S9, the specific surface area of the pure $NiCo_2O_4$ and $NiCo_2O_4/MnCo_2O_4$ are 113.7 and 176.8 m^2 g^{-1}, respectively. The adsorption cumulative volume of pores for the two samples is 0.366 and 0.69 cm^3 g^{-1}, respectively. The corresponding average pore sizes of the two samples are 6.5 and 14.97 nm (inserted in Fig. S9) calculated from adsorption isotherms. These results suggest that they have large surface area and high porosity, which is of huge benefits for the diffusion of electrolyte ions and accommodating the volume variation during the charge–discharge process. The unique architecture could increase the electrode/electrolyte contact area, provide sufficient active sites for redox reaction and numerous channels for efficient transport of electrons/ ions.

The electrochemical properties of $NiCo_2O_4/MnCo_2O_4$ as an anode material for LIBs are examined by cyclic voltammogram (CV) at a scan rate of 0.1 mV s^{-1} in the voltage window of 0.01-3.00 V versus Li/Li^+. As shown in Fig. 4a, in the first cycle, the pronounced cathodic peak centered at 0.61 V can be attributed to the reduction of $NiCo_2O_4/MnCo_2O_4$ to metallic Co, Ni and Mn (Eqns. 1 and 2). Two broad oxidation peaks are observed at 1.50 and 2.01 V in the anodic scan, corresponding to the oxidation of Mn to Mn^{2+}, Ni to Ni^{2+} and Co to Co^{3+} (Eqns. 3-6), respectively.[6,15] In the subsequent cycles, the main reduction peak shifts to 0.86 V and there is obvious intensity decline of both anodic and cathodic peaks after the first cycle. From the second cycle onwards, the CV curves overlap very well, indicating the good reversibility of the electrochemical reactions. Compared with the CV curves of $NiCo_2O_4$ electrode (Fig. S10), the oxidation peak centered at 2.24 shifts to 2.01 V, which reflects the intimate interaction between $NiCo_2O_4$ nanosheets and $MnCo_2O_4$ nanoparticles. This could reduce the electrode polarization and improve the charge-transfer kinetics, leading to a much higher capacity.[30] Based on the above analysis and previous reports,[6,15] the entire electrochemical process taking place can be classified as follows:

$$NiCo_2O_4 + 8Li^+ + 8e^- \rightarrow Ni + 2Co + 4Li_2O \quad (1)$$

$$MnCo_2O_4 + 8Li^+ + 8e^- \rightarrow Mn + 2Co + 4Li_2O \quad (2)$$

$$Co + Li_2O \leftrightarrow CoO + 2Li^+ + 2e^- \quad (3)$$

$$CoO + 1/3Li_2O \leftrightarrow 1/3Co_3O_4 + 2/3Li^+ + 2/3e^- \quad (4)$$

$$Ni + Li_2O \leftrightarrow NiO + 2Li^+ + 2e^- \quad (5)$$

$$Mn + 3Li_2O \leftrightarrow MnO + 6Li^+ + 6e^- \quad (6)$$

Fig. 4b shows the selected charge and discharge cycle curves of $NiCo_2O_4/MnCo_2O_4$ composite at a current density of 1000 mA g^{-1} in the range of 0.01-3.0 V. Among them, the discharge and charge capacities are 1646.2 and 1154.2 mA h g^{-1} in the first cycle, respectively, indicating a coulombic efficiency of 70 %. One can see from 3 to 100 cycles that an obvious decrease of the discharge capacity appeared, and then the discharge capacities gradually increased from 200 to 600 cycles. This trend matches well with the cycling performance shown in Fig. 4d. Fig. 4c shows the rate capability of the $NiCo_2O_4/MnCo_2O_4$ electrode. When the current density gradually increases from 50 to100, 200, 500 and 1000 mA g^{-1}, the corresponding average discharge capacities are 1133, 1128, 1060, 950 and 804 mA h g^{-1}, respectively. If the current density is reverted to 50 mA g^{-1} again, the discharge capacity retains to about 1375 mA h g^{-1}. These results demonstrate the $NiCo_2O_4/MnCo_2O_4$ has a great potential as a high-rate anode material for LIBs. To further probe the outstanding electrochemistry properties, the sample is then tested at 1000 mA g^{-1} (Fig. 4d). The discharge capacity

Journal Name RSCPublishing

ARTICLE

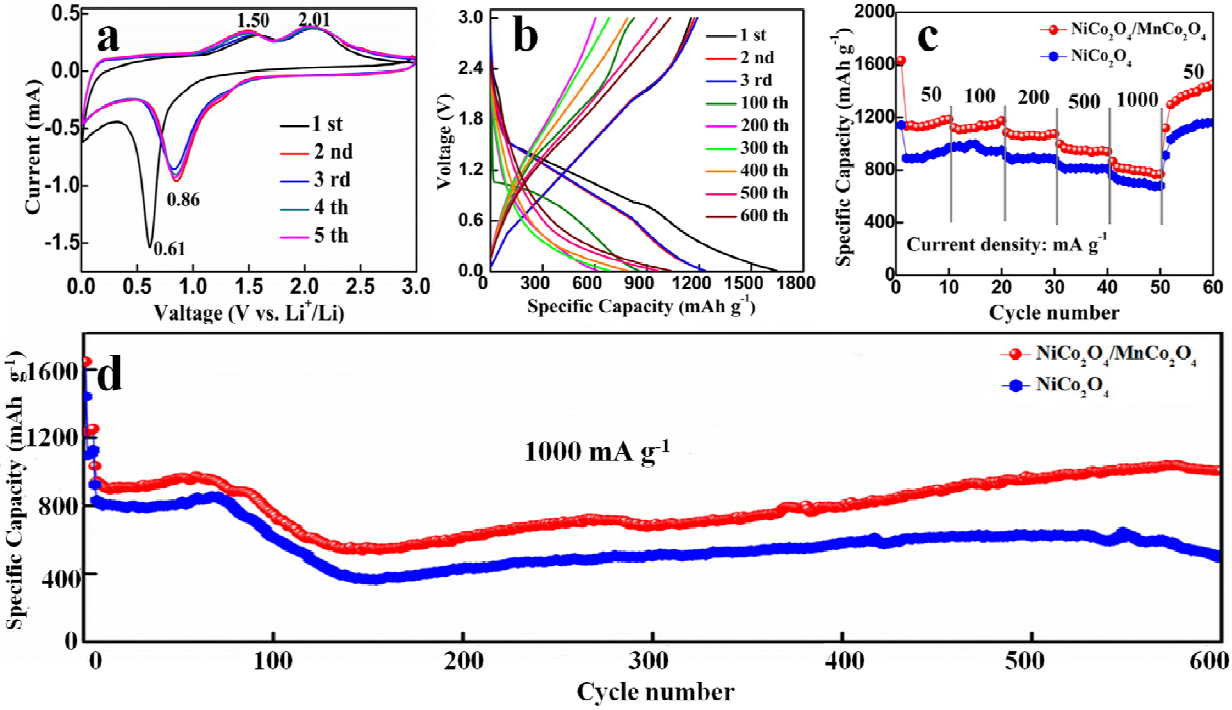

Fig. 4 (a) The first five cyclic voltammogram curves, (b) discharge-charge curves at 1000 mA g^{-1}, (c) rate capability test at various current densities and (d) cycling performance at 1000 mA g^{-1} of the hierarchical pours rose-like $NiCo_2O_4/MnCo_2O_4$.

slowly increases to 958.1 mA h g^{-1} after 60 cycles. Afterwards, the discharge capacity rapidly decreases to 544.3 mA h g^{-1} after 140 cycles. Finally, it slowly increases to 1009.2 mA h g^{-1} after 600 cycles. The $NiCo_2O_4/MnCo_2O_4$ displays an excellent cycling performance. The extra capacity might partly origin from the formation of SEI layer at the interface between the electrode and electrolyte, lithium-insertion reaction in acetylene black and interfacial storage.[17] The phenomenon of a gradual increase of capacity usually occur in transition metal oxides anodes materials, particularly nanostructured cobalt-based and manganese-based materials.[31,32] the synergistic effect between the $NiCo_2O_4$ nanosheets and $MnCo_2O_4$ nanoparticals possibly promotes the capacity change. The rose-like $NiCo_2O_4$ nanosheets with better electrical conductivity serve as the backbone to support the $MnCo_2O_4$ nanoparticals. The unique hierarchical pore structure would enhance the mechanical strength, provide enough space to buffer the volume expansion during the charge–discharge process. In addition, the "intercalation" induced capacitance behavior was caused by the intercalation of electrolyte into the mesoporous structure.[5] These characteristics are common in a large number of porous materials and cobalt-based materials.

We used CV curves to explain the "intercalation" induced capacitance behavior of the composite. Fig. S11a displays the CV curves of $NiCo_2O_4/MnCo_2O_4$ that cycles after 350 times at different sweep rates of 0.2, 0.5, 0.8 and 1.0 mV s^{-1}. The results show that the peak current density is not proportional to the square root of the sweep rate. A similar observation was reported in previous studies on electrode materials. Moreover, the capacitive controlled reaction could accelerate the diffusion of Li-ion and e^-, fundamentally improving the rate property. The faradaic process is found both in the bulk as a battery process and on the surface as pseudocapacitance. The capacitive effect of the battery system is calculated according to equations (7) and (8):

$$i = av^b \quad (7)$$

$$\text{Logi} = b \times \text{logv} + \text{loga} \quad (8)$$

in which the "i" is the current density, the "v" is the potential sweep rate, and the "a" and the "b" are adjustable parameters. Accordingly, for battery behavior, the b-value approaches 0.5 and the Li^+ insertion process dominates. In contrast to battery behavior, when the b-value is close to 1, the system is mainly controlled by capacitance. Fig. S11b shows the logi vs. logv plots at different oxidation or reduction state, indicating the b-value approaches 1. Therefore, the $NiCo_2O_4/MnCo_2O_4$ is mainly controlled by the capacitive process after 350 cycles, which leading to a fast Li^+ insertion/extraction (high rate property) and extended cycling life. [5,33-36]

Tab. 1 Cycling performance of the as-obtained $NiCo_2O_4/MnCo_2O_4$ and previously reported $NiCo_2O_4$ nanomaterials.

Type of materials	Current density (mA g^{-1})	First capacity (mAh g^{-1})	Cycle number	Remaining capacity (mAh g^{-1})	Ref.
$NiCo_2O_4$@ Au	100	1404.4	200	732.5	5
Fe_2O_3@ $NiCo_2O_4$	100	1311.4	100	1079.6	11
$NiCo_2O_4$/ 3DHPC	1000	1336	500	660	13
monodisperse $NiCo_2O_4$	800	1144	500	705	15
$NiCo_2O_4$ microflowers	500	~1760	100	720	24
CNTs/ $NiCoO_4$	200	-	200	~1200	17
$NiCo_2O_4$@ SnO_2	100	1623	100	765	37
$NiCo_2O_4$ nanobelt	500	1056	100	981	38
$NiCo_2O_4$ Nanosheets	100	-	50	767	39
Hollow $NiCo_2O_4$ nanosphere	2000	-	200	695	40
mesoporous $NiCo_2O_4$	485	-	400	1000	41
$Ni_xCo_{3-x}O_4$ nanosheets	500	~2150	200	844	42
rose-like $NiCo_2O_4/MnCo_2O_4$	1000	1646	600	1009	this work

The influences of different ratios of the active materials, acetylene black and CMC (such as 50 : 30 : 20 and 70 : 20 : 10) on the capacities of the product were evaluated (see Fig. S12 and Tab. 1). The results reveal that the $NiCo_2O_4/MnCo_2O_4$ (7: 2: 1) anode exhibits a lower discharge capacity of ~ 500 mA h g^{-1} after 400 cycles at 500 or at 1000 mA g^{-1}. AC and DC impedance spectra are performed in order to partly understand the synergetic effect between $NiCo_2O_4$ and $MnCo_2O_4$. As can be seen from Fig. S13a, the plots of the as-prepared $NiCo_2O_4/MnCo_2O_4$ and $NiCo_2O_4$ samples are composed of a quasi-semicircle at the high and middle frequency region and a slope line at the low frequency region. The semicircle can be attributed to the charge-transfer impedance (R_{ct}) at electrode/electrolyte interface, while the slope line might reflect the Warburg impedance (Z_w) induced by lithium diffusion in the electrodes. The R_{ct} values of $NiCo_2O_4/MnCo_2O_4$ are clearly smaller than that of $NiCo_2O_4$. The DC impedance spectra (Fig. S13b and Fig. S13c) reveal that the R_{dc} ($NiCo_2O_4/MnCo_2O_4$ composite) is smaller than that of the $NiCo_2O_4$. These results suggest that the composite electrode could effectively reduce the R_{ct} and R_{dc}, facilitating the electron transportation, and thus benefit the electrochemical performance.[6,13,24] The EIS spectra of the $NiCo_2O_4/MnCo_2O_4$ in the fully discharged states at 1000 mA g^{-1} after certain cycles (10 th, 50 th, 80 th and 100th) are shown in Fig. S13d. These Nyquist plots have similar shape characters with each other. The value of Rct (estimated from the depressed semicircles) for $NiCo_2O_4/MnCo_2O_4$ after 80 cycles is smaller than that after 100 cycles, which may result in the specific capacity decreasing from 886 to 750 mA h g^{-1}. Fig. S14 shows the morphology of $NiCo_2O_4/MnCo_2O_4$ composite electrode after ten cycles at a current density of 1000 mA g^{-1}. The Fig. S14a is the TEM image of the acetylene-black used as active material (only using acetylene-black) after ten cycles at 1000 mA g^{-1}. Compared with Fig. S14a and Fig. S14b, after ten charge-discharge cycles, the 3D porous rose-like $NiCo_2O_4/MnCo_2O_4$ (marked by the red frame) basically preserves the morphology and surface feature, suggesting its relative high morphology stability.

$NiCo_2O_4$ based materials for SCs also have been intensively studied. Recently, porous $NiCo_2O_4$ nanosheets electrode exhibited a specific capacitance of 400 F g^{-1} at 20 A g^{-1} and superior cycling stability over 5000 cycles.[39] Owing to the unique porous structure, the as-obtained $NiCo_2O_4/MnCo_2O_4$ composite is also suitable for applications as electrode for SCs. The pseudocapacitive properties of $NiCo_2O_4/MnCo_2O_4$ were further investigated by CV and galvanostatic charge-discharge measurements in three electrode configurations. Fig. 5a shows the typical CV curves of the $NiCo_2O_4/MnCo_2O_4$ electrode at various scan rates ranged from 10 to 50 mV s^{-1}. A couple of redox peaks are observed within the potential windows ranging from -0.1 to 0.45 V (vs. SCE) in 2.0 M KOH solution. These well-defined peaks mainly originates from Faradaic reactions related to M–O/M–O–ON (M represents Ni, Mn and Co ions) associated with anions OH^-, which indicates the typical pseudocapacitive characteristics of the as-prepared electrode materials. When the scan rate was increased from 0.2 to 1 mv s^{-1}, the shape of the CV curves is basically unchanged except for the small shift of the peak position. This result indicates that the as-obtained $NiCo_2O_4/MnCo_2O_4$ composite has excellent electrochemical reversibility and outstanding high-rate performances.

The galvanostatic charge-discharge curves were conducted in a potential range of 0-0.4 V at current densities of 1, 5 and 10 A g^{-1} to further evaluate the pseudocapacitive properties of the as-synthesized $NiCo_2O_4/MnCo_2O_4$, and the results are depicted in Fig. 5b. The discharge curves consist of a rapid potential drop due to the internal resistance and a sluggish potential decay coming from the Faradic redox reaction. The appearance of obvious voltage plateaus (at around 0.15–0.2 V) combined with

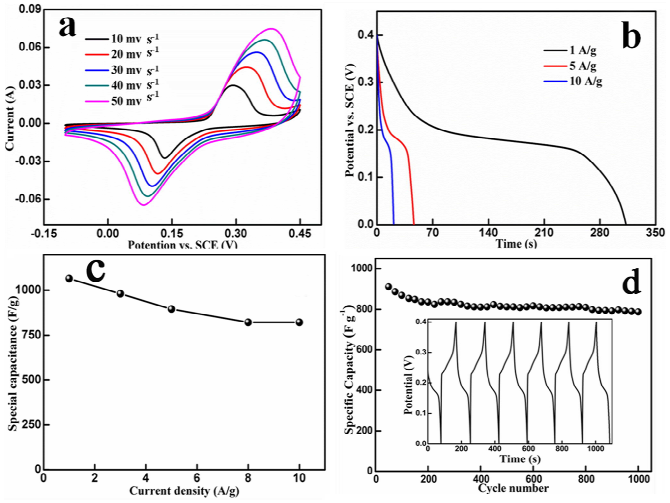

Fig. 5 (a) CV curves, (b) a comparison of the galvanostatic discharge voltage profiles, (c) the corresponding specific capacitance as a function of current density of the as-synthesized $NiCo_2O_4/MnCo_2O_4$ and (d) cycling performance at current densities of 5 A g^{-1} (inset: the galvanostatic charge/discharge cyclic curves of the first 6 cycles) and.

the CV curves reveal the pseudocapacitance behavior of the $NiCo_2O_4/MnCo_2O_4$ electrode. Its specific capacitance is evaluated by the formula C = I Δt / m ΔV, where I is the discharge current, Δt is the discharge time, m is the quality of the active material and ΔV is the voltage change. According to the above formula, the specific capacitances of the $NiCo_2O_4/MnCo_2O_4$ electrode are 1100, 870 and 760 F g^{-1} at current densities of 1, 5 and 10 A g^{-1}, respectively. The relationship between the specific capacitances and current densities of $NiCo_2O_4/MnCo_2O_4$ nanocomposites (Fig. 5c) has also been further investigated. It shows a ~ 23% specific capacitance loss with an increase in the current density from 1 to 10 A g^{-1}, revealing that they have good rate capability. The cycling stability of the hierarchical $NiCo_2O_4/MnCo_2O_4$ nanostructures is conducted by galvanostatic charge-discharge (Fig. 5d) at 5 A g^{-1} for 1000 cycles. The initial specific capacitance of $NiCo_2O_4/MnCo_2O_4$ electrode is 911.3 F g^{-1}. After 1000 cycles, the coulombic efficiency still remains 97 %. These excellent performances may be contributed by the unique 3D hierarchical structure of the $NiCo_2O_4/MnCo_2O_4$ material the synergistic effects between the $NiCo_2O_4$ nanoflakes and $MnCo_2O_4$ nanopaticles and the pseudo-capacitive contributions from the ultrathin mesoporous $NiCo_2O_4/MnCo_2O_4$. These may be in favor of ion permeability, resulting in the redox reaction rapidly taking place at high current densities.

4 Conclusions

In summary, 3D hierarchical porous rose-like nanoflake/$MnCo_2O_4$ nanoparticle composite was successfully fabricated by the decomposition of Ni-Co-Mn-based precursors at a moderate temperature (350 °C) in air, which have high reversible capacity of ~ 1009.2 mA h g^{-1} at 1000 mA g^{-1} even after 600 cycles as anodes material for LIBs; For the rate performance, they display better capacity retention, exceptionally high rate performance and ultra-long cyclic stability; When applied as electrode for supercapacitor, the specific capacitance of $NiCo_2O_4/MnCo_2O_4$ reaches 911.3 F g^{-1}. The excellent electrochemical performances may originate from the hierarchical porosity, the "intercalation" induced capacitance behavior and the favorable synergistic effect. The as-obtained 3D hierarchical porous rose-like $NiCo_2O_4/MnCo_2O_4$ composite exhibits outstanding electrochemical performances which enable them promising potential applications as material for the next-generation energy storage electrodes.

Acknowledgements

This research is financial support by the 973 Project of China (No. 2011CB935901), the National Nature Science Fund of China and Academy of Sciences large apparatus United Fund (nos. 21471091 and 11179043).

Notes and references

Key Laboratory of Colloid and Interface Chemistry, Shandong University, Ministry of Education, School of Chemistry and Chemical Engineering, Jinan 250100, P. R. China. Fax: +86 531 88366280; Tel: +86 531 88364543; E-mail: xulq@sdu.edu.cn.

1 M. Armand and J. M. Tarascon, *Nature,* 2008, **451**, 652.
2 P. G. Bruce, B. Scrosati and J. M. Tarascon, *Angew. Chem. Int. Ed.,* 2008, **47**, 2930.
3 S. L. Li, A. H. Li, R. R. Zhang, Y. Y. He, Y. J. Zhai and L. Q. Xu, *Nano Res.,* 2014, **7**, 1116.
4 N. N. Wang, H. Y. Xu, L. Chen, X. Gu, J. Yang and Y. T. Qian, *J. Power Sources,* 2014, **247**, 163.
5 J. Zhu, Z. Xun and B. G. Lu, *Nano Energy,* 2014, **7**, 114.
6 A. K. Mondal, D. Su, S. Chen, A. Ung, H. S. Kim and G. Wang, *Chem. Eur. J.,* 2015, **21**, 1526.
7 R. B. Wu, X. K. Qian, K. Zhou, J. Wei, J. Lou and P. M. Ajayan, *ACS Nano,* 2014, **8**, 6297.
8 A. H. Li, L. Q. Xu, S. L. Li, Y. Y. He, R. R. Zhang and Y. J. Zhai, *ano Research* 2015, **8** (2), 554–565.
9 Z. C. Bai, N. Fan, C. H. Sun, Z. C. Ju, C. L. Guo, J. Yang, Y. T. Qian, Nanoscale 5 (2013) 2442–2447.
10 R. R. Zhang, Y. Y. He and L. Q. Xu, *J. Mater. Chem. A,* 2014, **2**, 17979-17985.
11 G. Huang, L. L. Zhang, F. F. Zhang and L. M. Wang, *Nanoscale,* 2014, **6**, 5509.
12 M. C. Liu, L. B. Kong, C. Lu, X. M. Li, Y. C. Luo and L. Kang, *ACS Appl. Mater. Interfaces,* 2012, **4**, 4631.
13 L. Y. Wang, L. H. Zhuo, C. Zhang and F. Y. Zhao, *ACS Appl. Mater. Interfaces,* 2014, **6**, 10813.
14 Y. G. Li, P. Hasin and Y. Y. Wu, *Adv. Mater.,* 2010, **22**, 1926.
15 J. F. Li, S. L. Xiong, Y. R. Liu, Z. C. Ju and Y. T. Qian, *ACS Appl. Mater. Interfaces,* 2013, **5**, 981.
16 Y. N. Xu, X. F. Wang, C. H. An, Y. J. Wang, L. F. Jiao and H. T. Yuan, *J. Mater. Chem.*, 2014, **2**, 16480.
17 W. W. Liu, C. X. Lu, K. Liang and B. K. Tay, *Part. Part. Syst. Charact.,* 2014, **31**, 1151.
18 L. Huang, D. Chen, Y. Ding, S. Feng, Z. L. Wang and M. Liu, *Nano Lett.,* 2013, **13**, 3135.
19 N. Padmanathan and S. Selladurai, *Ionics,* 2014, **20**, 479.

20 T. Nguyen, M. Boudard, L. Rapenne, O. Chaix-Pluchery, M. J. Carmezim and M. F. Montemor, *RSC Adv.,* 2015, **5**, 27844.
21 T. Gao, H. Fjellvåg and P. Norby, *Anal. Chim. Acta,* 2009, **648**, 235.
22 C. F. J. Windisch, G. J. Exarhos and S. K. Sharma, *J. Appl. Phys.*, 2002, **92**, 5572.
23 C. C. Fu, G. S. Li, D. Luo, X. S. Huang, J. Zheng and L. P. Li, *ACS Appl. Mater. Interfaces,* 2014, **6**, 2439.
24 J. M. Xu, L. He, W. Xu, H. B. Tang, H. Liu, T. Han, C. J. Zhang and Y. H. Zhang, *Electrochim. Acta,* 2014, **145**, 185.
25 L. L. Li, Y. L. Cheah, Y. W. Ko, P. F. Teh, G. Wee, C. L. Wong, S. J. Peng and M. Srinivasan, *J. Mater. Chem. A,* 2013, **1**, 10935.
26 Y. Lei, J. Li, Y. Y. Wang, L. Gu, Y. F. Chang, H. Y. Yuan and D. Xiao, *ACS Appl. Mater. Interfaces,* 2014, **6**, 1773.
27 S. B. Wang, Y. D. Hou and X. C. Wang, *ACS Appl. Mater. Interfaces,* 2015, **7**, 4327.
28 K. Thongsuriwong, P. Amornpitoksuk and S. Suwanboon, *J Phys Chem Solids,* 2010, **71**, 730.
29 S. K. Li, Z. G. Wu, W. H. Li, Y. Liu, R. F. Zhuo, D. Yan, W. Jun and P. X. Yan, *CrystEngComm,* 2013, **15**, 1571.
30 N. N. Wang, J. Yue, L. Chen, Y. T. Qian and J. Yang, *ACS Appl. Mater. Interfaces,* 2015, **7**, 10348.
31 Y. J. Zhai, X. J. Ma, H. Z. Mao, W. W. Shao, L. Q. Xu, Y. Y. He and Y. T. Qian, *Adv. Electron. Mater.*, 2015, 1400057.
32 W. M. Chen, L. Qie, Y. Shen, Y. M. Sun, L. X. Yuan, X. L. Hu, W. X. Zhang and Y. H. Huang, *Nano Energy,* 2013, **2**, 412.
33 Z. Hu, L. X. Wang, K. Zhang, J. B. Wang, F. Y. Cheng, Z. L. Tao and J. Chen, *Angew. Chem. Int. Ed.,* 2014, **53**, 1.
34 Y. G. Wang, Z. S. Hong, M. D. Wei and Y. Y. Xia, *Adv. Funct. Mater.,* 2012, **22**, 5185.
35 T. Brezesinski, J. Wang, S. H. Tolbert and B. Dunn, *Nat. Mater.,* 2010, **9**, 146.
36 C. W. Kung, Y. H. Cheng, C. M. Tseng, L. Y. Choua and K. C. Ho, *J. Mater. Chem. A,* 2015, **3**, 4042.
37 G. X. Gao, H. B. Wu, S. J. Ding and X. W. Lou, *small,* 2015, **4**, 432.
38 A. K. Mondal, D. W. Su, S. Q. Chen, X. Q. Xie and G. X. Wang, *ACS Appl. Mater. Interfaces,* 2014, **6**, 14827.
39 A. K. Mondal, D. W. Su, S. Q. Chen, K. J. Kretschmer, X. Q. Xie, H. -J. Ahn and G. X. Wang, *ChemPhysChem*, 2015, **16**, 169.
40 X. Y. Yao, C. Y. Zhao, J. H. Kong, D. Zhou and X. H. Lu, *RSC Adv.,* 2014, **4**, 37928.
41 H. S. Jadhav, R. S. Kalubarme, C. -N. Park, J. Kim and C. -J. Park, *Nanoscale*, 2014, **6**, 10071.
42 F. C. Zheng, D. Q. Zhu and Q. W. Chen, *ACS Appl. Mater. Interfaces,* 2014, **6**, 9256.

Graphical Abstract

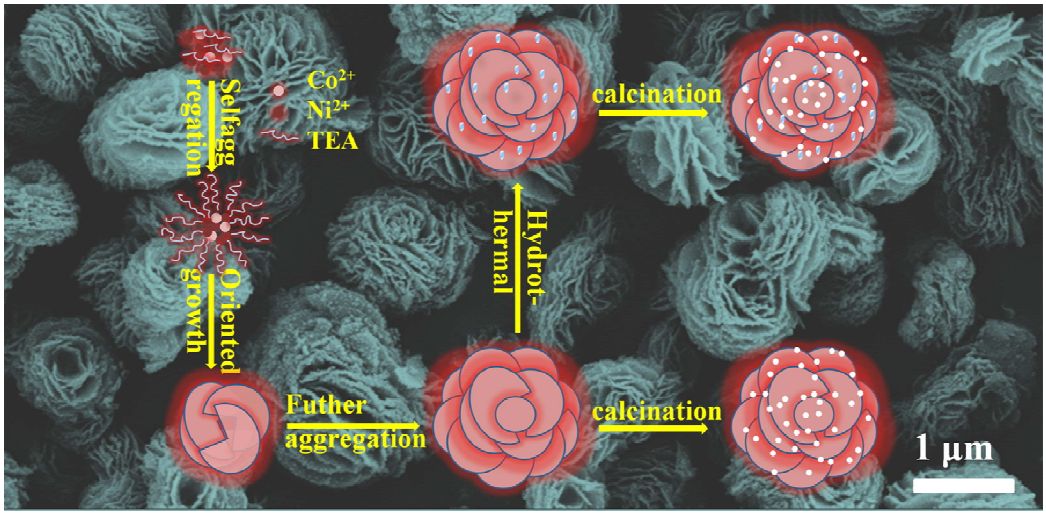

Three-dimensional hierarchical porous rose-like double binary metal oxide $NiCo_2O_4/MnCo_2O_4$ composites have been conveniently fabricated through a hydrothermal method follows an annealing treatment. The as-obtained product exhibits high specific capacity and long cycling stability (1009 mAh g^{-1} at 1000 mAh g^{-1} after 600 cycles) and excellent rate capability as anodes for lithium ion batteries; For supercapacitor application, the initial specific capacitance of $NiCo_2O_4/MnCo_2O_4$ is 911.3 F g^{-1}.